

Department of Physics and Astronomy
University of Heidelberg

Master Thesis in Physics
submitted by

Johanna Stratemeier

born in Duisburg (Germany)

2017

Automatic Needle Trajectory Selection for Brachytherapy of Liver Metastases

This Master Thesis has been carried out by Johanna Stratemeier at the
University Medical Centre Mannheim
under the supervision of
Prof. Dr. Jürgen Hesser

ABSTRACT

An emerging field for the application of brachytherapy is the treatment of liver metastases which are inoperable due to their small size or location. Because of the wide variety in anatomical circumstances, the treatment planning has to be highly customized for each patient requiring computational automation of the planning process. This work is the first that offers an automatic strategy to calculate potential needle trajectories. The aim is an automated algorithm which proposes the best entry points for a subset of needles reaching the whole volume of one metastasis while avoiding obstacles in between.

The algorithm was developed along one contrast enhanced CT data set. Perspective projections were used to calculate all trajectories from the skin to the tumor while avoiding the ribs and the blood vessels. On the basis of the projection images the best entry points were selected by their reachability of the tumor and minimal length trajectories.

A list of best entry points was produced while depending on several heuristically chosen parameters for the computation. This is the first and only method tackling this problem; hence a comparison cannot be made versus state of the art. Therefore, the analysis of function was conducted by a preliminary visual evaluation and internal comparison.

ZUSAMMENFASSUNG

Ein neuer Anwendungsbereich für Brachytherapie ist die Behandlung von Lebermetastasen, die aufgrund ihrer geringen Größe oder Lage inoperabel sind. Die Behandlung muss für jeden Patienten individuell geplant werden, was eine gute Automatisierung dieses Prozesses nötig macht. Im Rahmen dieser Arbeit wurde eine neue Methode zur Berechnung potentieller Nadeltrajektorien entwickelt. Das Ziel ist ein automatisierter Algorithmus, der die besten Einstichpunkte für ein Gruppe von Nadeln vorschlägt, die das gesamte Volumen einer Metastase erreichen können und dabei Hindernisse meiden.

Der Algorithmus wurde auf Basis eines kontrastunterstützten CT Datensatzes entwickelt. Um mögliche Nadeltrajektorien zu extrahieren wurden perspektivische Projektionen von Punkten im Tumor aus mit Blickrichtung Hautoberfläche gemacht, wobei die Rippen und

Blutgefäße die Hindernisse darstellten. Die Projektionsbilder wurden analysiert und die besten Einstichpunkte ermittelt. Kriterien hierfür waren die Erreichbarkeit des Tumors und möglichst kurze Trajektorien.

Die resultierende Liste von Einstichpunkten in Abhängigkeit von mehreren heuristisch gewählten Parametern wurde als sinnvoll bewertet. Da dies die erste Methode ihrer Art ist, gibt es keine anderen Ergebnisse mit denen sie momentan vergleichbar ist. Die Funktionsanalyse wurde daher durch visuelle Auswertung und internen Vergleich durchgeführt.

ACKNOWLEDGMENTS

First of all, I would like to thank my supervisor and head of the research group Prof. Dr. Jürgen Hesser for his constant guidance in my topic, support with ideas, criticism and optimistic confidence in my doing.

I would also like to thank Prof. Dr. Lothar Schad for agreeing to be my second adviser.

Many thanks are owed to my colleagues for their professional help and supportive friendship in and outside office hours. I wish to express special gratitude to Katharina Jerg for repeated editorial revision and Matthias Brandt for patient assistance with computational issues.

At last, i want to give thanks to my parents and family who give me strength at any time i need it.

CONTENTS

1	INTRODUCTION	1
2	THEORY	3
2.1	Ionizing Radiation	3
2.1.1	Radioactive Sources	3
2.1.2	X-Ray Sources	5
2.1.3	Interactions of Photons with Matter	5
2.2	Radiobiology	6
2.3	Treatment Modes	8
2.3.1	LDR	9
2.3.2	HDR	9
3	STATE OF THE ART	11
3.1	General Treatment Planning	11
3.2	Image Guidance	12
3.3	Needle Planning	12
3.3.1	Centroid Voronoi Tesselation Algortihm	13
3.3.2	Non-parallel Needle Configurations	14
3.3.3	Occluded Volumes	16
3.4	Needle Insertion	17
3.5	Application to Liver Metastases	18
4	MATERIALS AND METHODS	21
4.1	Medical and Anatomic View	21
4.2	Workflow	21
4.3	Input Data	24
4.4	Object Segmentation	24
4.5	Object Processing	25
4.5.1	Tumor Representation	25
4.5.2	Ribs' Object	26
4.6	Projection	27
4.7	Calculation of Trajectories	29

4.8	Weighting and Needle Subsets	30
4.9	Projection Plane to Patient Surface	31
4.10	Output Data	31
4.11	Evaluation	32
4.11.1	Computation Time	32
4.11.2	Workflow Output	32
5	RESULTS	33
5.1	Object Processing and Projection	33
5.2	Trajectory Calculation and Subsets	36
5.3	Calculation Time	37
6	DISCUSSION	39
6.1	Tumor Projection	39
6.2	Ribs' Extension Factors	40
6.3	Skin Projection	40
6.4	Computation Time	41
6.5	Limitations	41
6.6	Automation	41
7	CONCLUSION AND OUTLOOK	43
	BIBLIOGRAPHY	45

ACRONYMS

ABS	American Brachytherapy Society
CT	Computer Tomography
CTV	Centroid Voronoi Tesselation
DICOM	Digital Imaging and COmmunications in Medicine
DSB	Double-Strand Breaks
GLM	Open Graphics Library Mathematics
HDR	High Dose Rate
HU	Houndsfield Unit
LDR	Low Dose Rate
MRI	Magnetic Resonance Imaging
NifTI	Neuroimaging Informatics Technology Initiative
NPIP	Needle Planning by Integer Programming
OpenGL	Open Graphics Library
PDR	Pulsed Dose Rate
PET	Positron Emission Tomography
PTV	Planned Target Volume
RCO	Rotate-Cannula-Only
STL	Stereolithography
TGA	Truevision Graphics Adapter
TRUS	TransRectal UltraSound

INTRODUCTION

Ranking 5th in the cancer incident statistics for men and a high mortality rate of 95 % make liver cancer the worldwide second most common cause of death from cancer, according to the WHO [1]. The liver is also a very regular site for metastases from colorectal, breast and lung cancer due to its dual blood supply. While 50 % – 60 % of the metastases spread from colorectal cancer are found to be in the liver only about 15 % of all liver metastases are surgically removable because of their number, size, location or the patient's health condition [2]. Therefore, brachytherapy has evolved as a minimal invasive treatment option often with the goal of tumor control and a palliative approach rather than cure.

Brachytherapy is a form of radiation therapy for cancer in which the radiation source is placed next to or inside the target region via needles or applicators. It has been widely used for prostate, cervix and breast cancer [3] in combination with other treatment options such as chemotherapy or external beam radiation. In contrast to locally ablative therapies like radio-frequency ablation (RFA) or Laser-induced thermotherapy (LITT) there are no restrictions to the size and shape of the target volume and no problems with the cooling effect of vessels nearby. The steep dose gradient achievable by brachytherapy sparing the surrounding healthy tissue is an important advantage towards external radiation therapy. Nevertheless, its use is limited to an intermediate number of metastases [4].

The radiation delivery has a wide variety from permanent seed implantation with a low dose rate common for prostate cancer to interstitial temporary application with one or a few treatment sessions fitting best for liver metastases [5]. A treatment with high dose rates is generally planned on the basis of an image data set of the patient acquired before the actual procedure. The target region and structures at risk are identified and a dose is prescribed by a radiation oncologist. Needle placement, dose objectives and dwell-time for the radiation sources are planned with these input parameters. Algorithms for an automation of the planning step are subject to current research. The overall aim is to provide a satisfactory dose coverage of the target volume while sparing healthy tissue from mechanical and radiation damage, which can cause major side effects for the patient. Calculation time, imaging tech-

nique, necessary number of needles, accuracy, robustness, degree of automation, handling and many others are parameters that vary. The automation of planning leads to the consequential step to automatize the intervention process as well in form of a robot. It presents the opportunity to improve accuracy of needle placement and offers a new dimension of needle handling [6]. It could lead to a broader use of brachytherapy since the outcome of the treatment does not depend so much on the operators experience any more.

This work focuses on a new identification method of potential needle subsets for brachytherapy of liver metastases. A dose planning algorithm has to be appended for the final selection. The aim is to reduce trauma by avoiding structures like ribs and major blood vessels while choosing the subset of needles by shortest distance between entry zone and target region. As opposed to other algorithms like Needle Planning by Integer Programming [7], perspective projections in OpenGL are used.

This work is structured as follows: First, an introduction to brachytherapy and its use for cancer treatment is given. The current state of the art concerning different aspects of brachytherapy planning and application is presented thereafter. In chapter 4 the conditions and input data for this algorithm are explained, followed by the exposition of the algorithm's workflow and output. Chapter 5 presents the results of the routine which are further discussed in chapter 6. A conclusion and outlook on implementation and future work is given in the last chapter.

2

THEORY

This chapter gives an overview of the theory of brachytherapy. The ionizing radiation, its sources and physical principles are explained first. The biological effect and the resulting treatment modes are discussed in section 2.2 and 2.3.

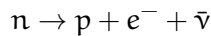
2.1 IONIZING RADIATION

Ionizing radiation is electromagnetic radiation that carries enough energy (keV – MeV) to ionize an atom or molecule. For further explanation, the description of the electromagnetic radiation as photons is chosen, either as x-rays or γ -rays depending on the source.

2.1.1 *Radioactive Sources*

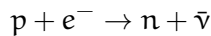
A typical source for ionizing radiation used in brachytherapy is $^{192}\text{Iridium}$ [8]. Therefore, it is selected as an example to discuss radioactive sources. There are two decay modes for ^{192}Ir : β^- decay and electron capture.

β^- decay is the process of a neutron transitioning into a proton under irradiation of an electron and an antineutrino:



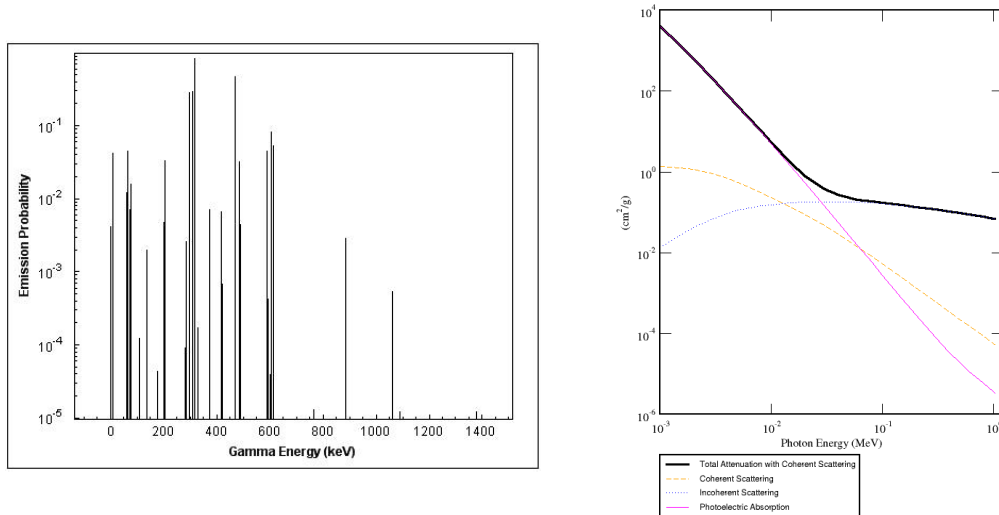
The energy freed by the transition is carried by e^- and $\bar{\nu}$. The daughter nuclide of the decay might be in an excited state and can release the excitation energy by γ -ray emission or internal transition [9].

Electron capture is a transition from a proton with an electron to a neutron plus an antineutrino:



Independently of the specific decay process, the activity of a source can be described by

$$A(t) = A_0 \cdot e^{-\mu t}, \quad \text{with } A_0 = A(t=0)$$

(a) Gamma spectrum of ^{192}Ir [11]

(b) Photon attenuation in water [12]

Figure 1: Characteristic gamma spectrum of the ^{192}Ir decay (a) and the corresponding energy range for photon attenuation in water (b) are shown here. The different processes taken part in the attenuation are represented by the coloured lines: Rayleigh scattering as the coherent scattering, Compton scattering as the incoherent scattering and the photoelectric effect are involved in the attenuation process in this energy interval. Water is picked as a representative for tissue in general.

with μ as the decay constant. The half-life is defined as the time at which the initial activity A_0 has decreased to its half:

$$A(T_{1/2}) = \frac{A_0}{2}$$

$$\Rightarrow T_{1/2} = \frac{\ln(2)}{\mu}.$$

^{192}Ir branching ratio of the β^- decay mode is 95.24 % while the one for the electron capture decay is 4.76 % [10]. The emitted characteristic γ -spectrum is shown in figure 1a. The average energy is 397 keV. As characteristics for the use as a brachytherapy source, the average energy of the γ -rays, the half-life of the radioactive isotope and the ability to seal the nuclide in a practical geometry are important. Depending on the treatment site and mode, the demands on the source differ. Further discussions are therefore postponed to section 2.3.

2.1.2 X-Ray Sources

Besides radioactive materials also electronic sources for ionizing radiation can be used in brachytherapy. It eliminates problems like the limitation to half-lives, leakage, radioactive waste, radiation dose to staff, storage and many more. The challenge is the source dimension [13]. An x-ray tube contains a cathode and an anode in a vacuum. Electrons are released by a hot cathode and accelerated towards the anode. In the electric coulomb field of the anode, the electrons get deflected and slowed down. Energy is irradiated as Bremsstrahlung in a continuous spectrum of x-rays. The additional characteristic x-ray emission is material specific: a fast electron knocks out an electron of the atom shell. An electron from an outer shell fills the vacancy and irradiates the difference in energy as a photon.

2.1.3 Interactions of Photons with Matter

Figure 1b shows the attenuation of photons in water for the corresponding energy interval to the ^{192}Ir γ -spectrum. Three processes depending on the photon energy take place when incoming photons interact with electrons of the atom shell:

- *Coherent Scattering* is an elastic scattering of the photon independent of the energy E_{photon} .
- *Photoelectric Absorption* describes a process where the energy of the photon is used to enable an electron to escape the nucleus attractive potential of the atom, while the difference between ionization and photon energy is transformed into kinetic energy of the freed electron.

$$E_{\text{photon}} = E_{\text{binding}, e^-} + E_{\text{kin}, e^-}$$

- *Incoherent Scattering* is an inelastic scattering of a photon with an electron. The photon transfers only a part of its energy to the electron which is thereupon ejected from the nuclear shell.

$$E_{\text{photon}} = E_{\text{binding}} + E_{\text{kin}, e^-} + E'_{\text{photon}}$$

The freed electrons from the photoelectric absorption and the incoherent scattering primarily cause the damaging effect to the tissue described in section 2.2.

2.2 RADIobiology

The aim in cancer treatment with ionizing radiation is to induce cell death by damaging the DNA. Secondary electrons can interact directly and indirectly with the DNA (figure 2a). During direct interaction electrons ionize or excite molecules in the DNA. This can cause single- or double-strand breaks. If the electron interacts with another molecule in the cell, for example water, the molecule transforms into a free radical. It has an unpaired electron which makes it highly reactive. If the radical is within a diffusion radius of a few nm to the DNA, it reacts with the molecules and causes a single-strand break. This is called indirect interaction.

Because of repairing mechanism of the DNA these damages do not necessarily lead to cell death. Single-strand breaks or even double-strand breaks (DSB) if apart far enough within the DNA strand can be repaired by using the counter part of the damaged strand as a template. However, if a DSB occurs within a close range, the DNA double-strand is split in two fragments.

Its ends can

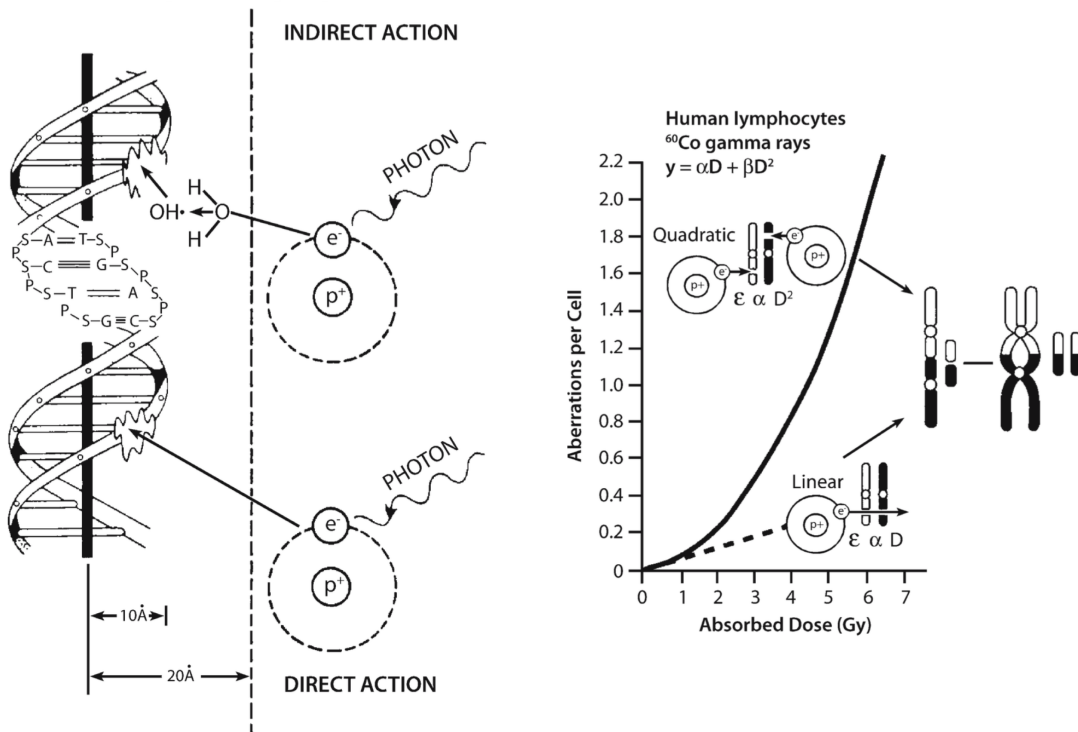
- rejoin to the original constellation. No permanent damage is done to the cell.
- not rejoin and stay in fragments causing aberrations for the next mitosis.
- rejoin with fragments of other damaged chromosomes. This damage is called exchange aberration and is lethal to the cell.

The relationship of aberrations per cell to the absorbed dose is shown in figure 2b. As an example a ^{60}Co source for the γ -rays in application on human lymphocytes cells are chosen. Aberration is a result of a DSB, at low doses the relating curve is linear because it is most probable that the DSB is caused by the same electron. At higher doses, meaning a greater number of electrons potentially damaging the DNA, the relationship is quadratic. The probability that a DSB is caused by two different electrons is much higher than by only one. Combining both processes, the overall frequency of aberration per cell is given by the linear-quadratic function

$$y = \alpha D + \beta D^2,$$

where D is the dose, α and β are constants. This simple model leads to the estimate of the surviving fraction by

$$S = e^y = e^{\alpha D + \beta D^2}.$$



(a) "Direct and indirect actions of radiation. The structure of DNA is shown schematically; the letters S, P, A, T, G, and C represent sugar, phosphorus, adenine, thymine, guanine, and cytosine, respectively. In direct action, a secondary electron resulting from absorption of an X-ray photon interacts with the DNA to produce an effect. In indirect action, the secondary electron interacts with a water molecule to produce a hydroxyl radical (OH^\bullet), which in turn diffuses to the DNA to produce damage. The DNA helix has a diameter of about 2 nm. It is estimated that free radicals produced in a cylinder with a diameter double that of the DNA helix can affect the DNA. Indirect action is dominant for sparsely ionizing radiation, such as X-rays." [14]

(b) "The frequency of interchange-type chromosomal aberrations (...) is a linear-quadratic function of dose because the aberrations are the consequence of the interaction of two separate breaks. At low doses, both breaks may be caused by the same electron; the probability of an exchange aberration is proportional to dose (D). At higher doses, the two breaks are more likely to be caused by separate electrons. The probability of an exchange aberration is then proportional to the square of the dose (D^2)."^[14]

Figure 2: Scheme of direct and indirect action of secondary electrons to the DNA (a) and its effect on the aberration of the cell (b).

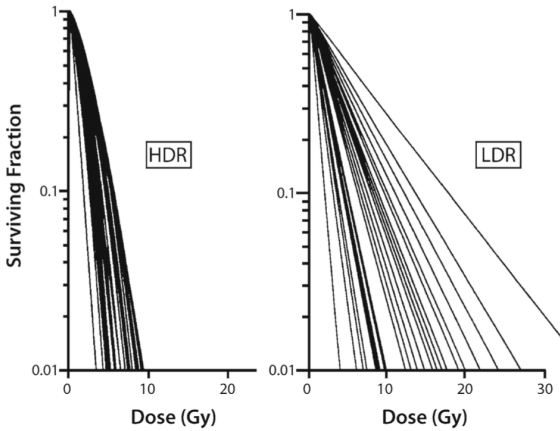


Figure 3: "Dose survival curves at high dose rate (HDR) and low dose rate (LDR) for a large number of cells of human origin cultured in vitro. Note that the survival curves fan out at low dose rate because, in addition to a range of inherent radiosensitivities (evident at HDR), there is also a range of repair times of sublethal damage." [14]

Figure 3 shows the survival rate to dose curves of many different cell types found in the human body. The measurement of the cell survival is done in vitro. For low dose radiation it has to be considered that it takes more time to deliver the same total dose. This provides time to the DNA repairing mechanism and causes a further fanning out of the curves for the treatment with low dose rates. Another contribution to the fanning out for both dose rates is the difference in radiosensitivity of the cells. The discussion of specific cell characteristics in radiobiology is beyond the scope of this work and can be found in Saha [9].

2.3 TREATMENT MODES

Using this knowledge about the biological effect of different dose rates, various treatment modalities of brachytherapy have evolved. The dose rates are categorized into

LOW DOSE RATE (LDR) with $0.4 - 2 \text{ Gy/h}$.

MEDIUM DOSE RATE (MDR) in a range of $2 - 12 \text{ Gy/h}$.

HIGH DOSE RATE (HDR) with doses $> 12 \text{ Gy/h}$.

LDR and HDR are the common treatment modes and their implementation will be discussed in the following.

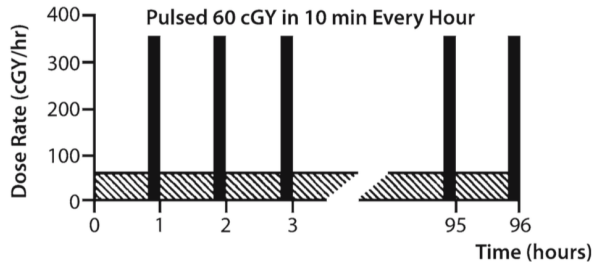


Figure 4: Scheme of the substitution of a low dose rate treatment with 60 cGy/h delivered continuously over 96 hours by a pulsed dose rate summing up to the same total dose per hour. [14]

2.3.1 LDR

Historically, the classical brachytherapy treatment is the LDR seed implantation [3]. Radioactive seeds with a short half-life are implanted directly into the target region and remain there. This leads to a continuously decreasing low dose rate delivered over several days. Surrounding normal tissue might be able repair itself depending on the specific dose rates and distance. The decrease in radiation also accounts automatically for the expected tumor damage. A problem can be the fraction of radiation leaving the patient's body and causing radiation exposure to the hospital staff and relatives. Also the surgeons are exposed to radiation during implantation. Sources used for this procedure are ^{125}I , ^{103}Pd and ^{198}Au with very different half-lives of 59.6, 17 and 2.7 days. Inpatient treatment is necessary to avoid risks for the patient's environment. The common usage of the LDR seed implantation over decades provides a broad data basis for standardization of the treatment procedure and exploration of risks and potentials. LDR brachytherapy can also be delivered interstitially and intracavitory via needles, catheters or applicators.

2.3.2 HDR

Difficulties with limited source availability and the radiation exposure to by-standers encouraged the development of Pulsed Dose Rates (PDR). The aim is to deliver the same total dose, but in pulses of irradiation with a higher dose rate (figure 4). The delivery of the PDR brachytherapy is realized with computerized after loaders which shield the environment from the sources and position the source tubes precisely at the precomputed dwell locations for a specific dwell time.

High Dose Rates (HDR) also can be delivered independently from previous LDR considerations in only one or a few fractions. Hospitalization time is shorter or even unnecessary and the staff is spared from radiation exposure. Since higher doses are delivered at once the planning of the treatment has to be individualized and a high standard of quality assurance is vital. The steep dose gradient in connection with the immense damage to the tissue in the irradiated volume carries great potential to eradicate cancer cells very fast but also to damage normal tissue if the source is not placed precisely.

Table 1 summarizes advantages and disadvantages of LDR and HDR brachytherapy treatments. The final decision with which dose rate a patient is treated depends on many factors like the cancer cell type, the site of the tumor, the hospital's equipment, experience of the physician and physicist, availability of radioactive sources and many more.

	LDR	HDR
Advantages	> 100 years of experience Standardized treatment plan, time and doses Maximum of two insertions	Outpatient treatment No staff exposure Dose optimization to normal tissue
Disadvantages	Inpatient treatment Radiation exposure to staff Limited sources available	Intense quality assurance Caution with normal tissue Intense physician/physicist time

Table 1: Some advantages and disadvantages for LDR and HDR Brachytherapy [15]

STATE OF THE ART

Brachytherapy has evolved with the developments in imaging techniques and planning systems over the last decades. Of major interest are methods which allow fast or even online adjustments to the treatment plan compensating for inaccuracies of needle insertion for example. Since liver cancer is a rather new target for brachytherapy, some methods are discussed by means of classical application site.

Firstly, general treatment planning routines for brachytherapy and possibilities of image guidance are discussed. Then the focus is set on the planning of needle trajectories and their configuration as a set. The alternative option of drilling the needle into the tissue is presented in section 3.4. Finally, the experience of brachytherapy of liver metastases is documented.

3.1 GENERAL TREATMENT PLANNING

Polo et al. [16] present three different kinds of modern planning systems which are defined by the American Brachytherapy Society (ABS) [17]. The discussed application is permanent seed prostate brachytherapy for which the classical approach is pre-planning the treatment session on the basis of medical imaging a few days in advance.

The first system is the intraoperative pre-planning. The planning is performed right before the procedure in the treatment room. In this case, the patient does not have to attend an additional appointment for the treatment planning a few days earlier and there is no need for patient repositioning according to image registration of planning and operating images. The outcome of the dosimetric comparison to classical pre-planning proofs the intraoperative pre-planning with transrectal ultrasound (TRUS) to be favourable [18].

The interactive planning enhances the intraoperative pre-planning by using the continuous information about needle position during the implantation to refine the initial treatment plan. Shanahan et al. [19] find the dosimetric results of intraoperative pre-planning and the hybrid technique with interactive planning to be comparative, whereas the pre-planning time, total procedure time and the number of needles are significantly reduced. One of the shortcom-

ings of this technique is that the needle is used as an indicator for the adjustment of the plan and not the seed itself.

Dynamic dose calculation is in general similar to the interactive planning but the seed position is tracked which considers the movement of the seed and the influence of the surrounding on the position where the dose is truly deposited. Kuo et al. [20] approach the issue of tracking the seeds by detecting fiducial markers and matching the seeds by reconstruction. The dosimetric outcome is comparable to the intraoperative planning method carried out by the same group.

3.2 IMAGE GUIDANCE

For classical tumor sites like prostate and cervix cancer different methods of image guidance have been implemented. An advantage of these locations is the possible use of body cavities for applicators and image guidance system. For example the transrectal ultrasound guidance (TRUS) first allowed the application of brachytherapy without an open surgery in 1983 [21] and it has become a standard of practise ever since [3]. A drawback of ultrasound is that the tumor cannot be easily visualized. Whereas MRI has a much better contrast in soft tissue, but the implementation into the clinical routine of brachytherapy is much more difficult due to a usually off-site location of the MRI scanner [22]. Only a small minority of clinics with an interventional MRI (iMRT) are facilitated for MRI-guided brachytherapy [23]. An approach to combine these two image modalities by registering the MRI image to the ultrasound image seems to be promising [24]. Brachytherapy with fluoroscopic CT-guidance [25] is still a feasible alternative if an MRI scanner is not available, but the iMRT is considered the future image guidance system for brachytherapy on liver metastases [8].

3.3 NEEDLE PLANNING

The planning of the needle trajectory for interstitial Brachytherapy is classically done manually with the help of a 3D rendering program [26] in a pre-planning session. It is subject to the present research to automatize the process of computing possible needle trajectories and the connected dose optimization.

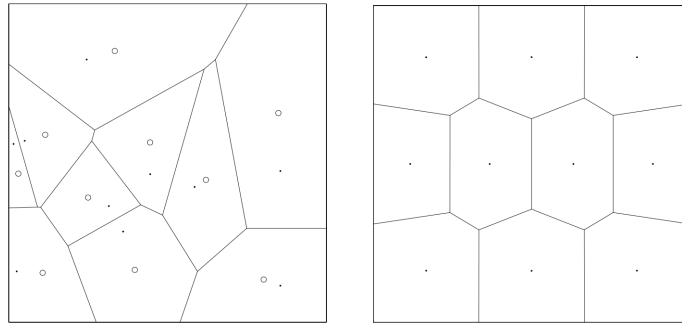


Figure 5: "On the left, the Voronoi regions corresponding to 10 randomly selected points in a square; the density function is a constant. The dots are the Voronoi generators and the circles are the centroids of the corresponding Voronoi regions. Note that the generators and the centroids do not coincide. On the right, a 10-point centroidal Voronoi tessellation. The dots are simultaneously the generators for the Voronoi tessellation and the centroids of the Voronoi regions." [28]

3.3.1 Centroid Voronoi Tessellation Algorithm

As an approach to uniformly distribute catheters in space, Poulin et al. [27] use the Centroid Voronoi Tessellation (CVT) algorithm [28]. The 3D contour of the Planned Target Volume (PTV) of the prostate or breast is projected in 2D space. The projected contour is used as the constraint for optimization. The number of generating points is chosen to be equal to the desired number of catheters. By the characteristic that the generators are also the centroid points of the Voronoi cell in CVT (Figure 5), it assures that the points are uniformly distributed over the target region. Afterwards, the needle trajectories are reconstructed in 3D in a parallel configuration. The Inverse Planning Simulated annealing algorithm (IPSA) optimizes time and dwell position for the proposed needle constellation.

Eight clinical cases were randomly chosen to study the parameters of the CVT algorithm and the dosimetric outcome in connection with the number of needles needed. Down to a prefixed number of the CVT algorithm showed an equal or better dosimetric outcome than in the actually applied treatment. Parameters of the CVT are the number of sampling points and the iterations. Since there is no effect of these parameters on the dosimetric indices found, they are fixed to 2500 sampling points and 100 iterations. The computing time for 10 treatment plans for the same case (with the number of catheters ranging from 9 to 18) is 90 s, while 93 % of that time are used for the dosimetric optimization with IPSA.

3.3.2 Non-parallel Needle Configurations

In times where no inverse planning tools were available yet, mechanical templates for parallel needle configurations for brachytherapy were useful to ensure a uniform conformal dose to the target volume. Cunha, Hsu, and Pouliot [29] tested three different needle patterns with the aim of minimal changes to the clinical routine, equal dosimetric results, but less injuries to the critical structures surrounding the prostate for 10 patient data sets. The patients are treated with HDR brachytherapy in a parallel needle set-up and inverse planning with IPSA. The number of needles and dosimetric conditions are kept the same for the hypothetical plans as they were used for the actual treatment. A conical, bi-conical and firework needle configuration are chosen as patterns (Figure 6) and plans are computed for each of them. The study shows that clinically acceptable plans can be achieved with these alternative needle patterns and they are easy to implement into the clinical routine. In the outlook of robot-assisted and image-guided brachytherapy, non-parallel needle configurations are mechanically feasible and various patterns should be exploited in order to optimize dose delivery to the target volume while sparing critical structures from radiation and mechanical damage.

On this basis, Siauw et al. [7] developed a planning algorithm for skew-line needle trajectories called "Needle Planning by Integer Programming" (NPIP) consisting of three steps: Generating a set of candidate needles, selecting a needle subset, and dose planning. The first two steps are illustrated in figure 7.

An entry zone for the needles is predefined and randomly sampled points in this zone are selected as starting points e_i of a line segment. The target object is represented by its contour points c_j . All the points t_{ij} are then computed as the point of intersection of a line defined by e_i and c_j with the top slice of the image data. The set of all potential needle trajectories are now the connecting line segment between randomly sampled points on the entry zone and the set of computed points t_{ij} which do not intersect a forbidden object.

Criteria for a needle subset is that it is collision free, meets the dose objectives and contains as few needles as possible. For solving this optimization problem the concept of a binary integer program is used. The condition of dose coverage is transferred into the condition of spatially covering the target volume by a user-defined parameter δ which gives the radius around a needle considered covered by it.

The algorithm was tested on 18 patient data sets. For all of them a needle configuration was

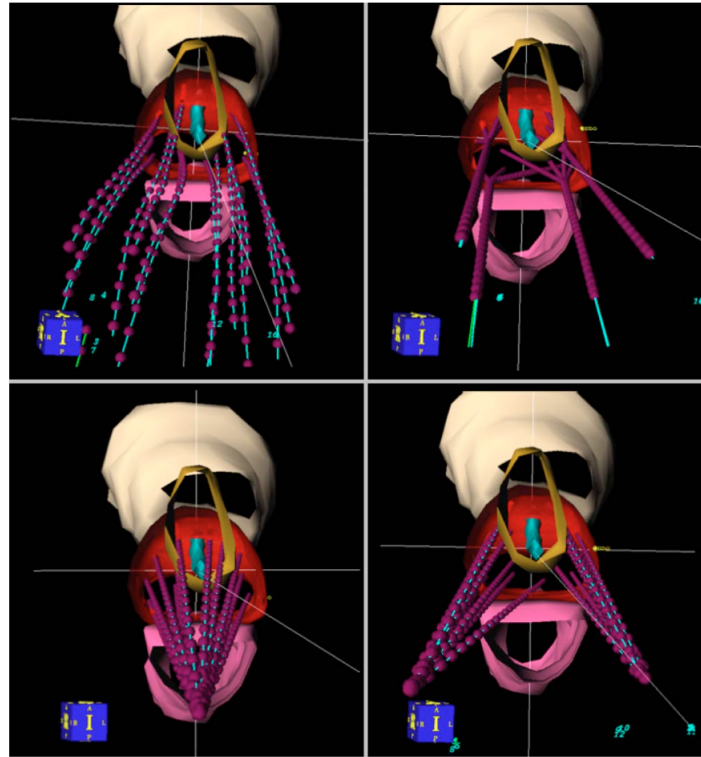


Figure 6: "Here the bladder is in the upper portion of the image, followed by the contoured bulb/C-SNB, the prostate, the urethra, and finally the rectum in the lower portion. The catheters enter from the lower foreground the patient's perineum and proceed into the page. Upper left: A standard implant used in the actual patient treatment. Upper right: The same patient, but with a hypothetical fireworks distribution. Lower left: A single-cone catheter pattern. Lower right: A bi-conical catheter pattern." [29]

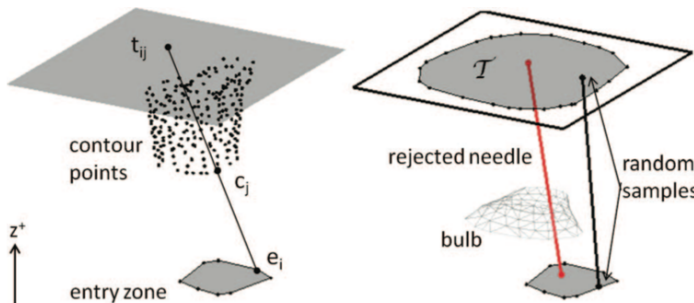


Figure 7: "A set of candidate needles was generated according to the anatomy of the patient. Given the vertices of an entry zone, E , and the contour points of the prostate, C , a set of points was computed, T , such that $t_{ij} \in T$ was the intersection of the line containing $e_i \in E$ and $c_j \in C$ with a plane perpendicular to the z -axis at the most superior slice of the target. The convex hull of T was called T . A needle was generated by randomly sampling a point in E , the convex hull of E , and in T , and generating a line connecting them. Needles that intersected a healthy structure were removed." [7]

found that is collision-free, meets the dose objectives and avoids critical structures. A weak point however is to find the right input parameters, especially the distance parameter δ . The number of needles used in a plan is linearly dependent on the size of the target volume because of δ . If δ is chosen to be too large, only one needle can cover the whole target volume according to the algorithm section of selecting a needle subset. Subsequently, no satisfying dose plan can be made. But if δ is too small, more needles than necessary are used for the dose planning and the result is worse compared to classical planning and implantation. However, if this problem can be solved in the future, the algorithm could be implemented in a brachytherapy robot for automatic treatment planning.

3.3.3 Occluded Volumes

Another problem in brachytherapy planning is the inaccessibility of a partial volume of the target if critical structures are strictly avoided. Alternative needle patterns diminish its extend, but cannot always solve it. Garg et al. [30] conducted an "Exact Reachability Analysis for Planning Skew-Line Needle Arrangements for Automated Brachytherapy" to improve the selection of needle subsets. This work is based on the NPIP algorithm discussed in section 3.3.2 and aims to supplement it. In NPIP occluded volumes are assumed to be small enough to be ignored and still get a satisfactory result for meeting dose objectives. By identifying the occluded volumes, the needle selection can be adapted such that needles are strategically positioned around this volume and therefore ensure dose coverage.

Figure 8 shows the visualization of an exemplary scene with an entry zone, the avoidance volume and the target volume modelled as convex polyhedra. The algorithm casts shadow cones from all extreme points of the entry zone onto the target volume while the cone edges intersect the contour points of the avoidance volume. The intersection of all the shadowed partial volumes in the target is the occluded volume. It cannot be reached by a straight needle originating anywhere in the entry zone and not intersecting the avoidance volume. This procedure was tested on 18 patient data sets. 11 of them had an occluded volume with a size ranging from 0.01 % and 4.3 % of the target volume.

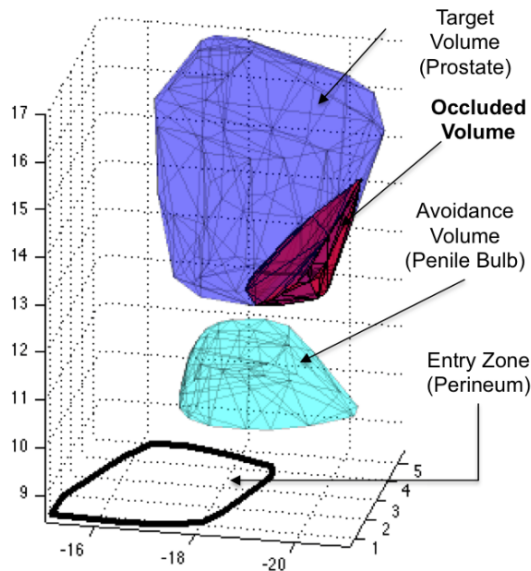


Figure 8: "This figure shows a target volume (blue), an avoidance volume (cyan), and an entry zone (black), which represent the prostate, penile bulb, and perineum, respectively, in case of prostate brachytherapy. This study develops an exact algorithm for finding an occluded volume (red), which is the region inside the target volume that cannot be reached by any straight line originating in the entry zone without intersecting the avoidance volume, or showing that no such volume exists. (...) " [30]

3.4 NEEDLE INSERTION

The inaccuracy of the final needle tip position is not only due to the operator's hand, but also the deformation of the tissue under the pressure of the piercing needle tip. It is shown, that rotating the needle during insertion can improve the accuracy [31]. The downside is an increase of damage to the tissue passing through. A Meltsner, Ferrier, and Thomadsen [6] used two different shapes of needle tips with various insertion and rotation speed of the needle to find a trade-off configuration between accuracy and damage for the use in a brachytherapy robot. Figure 9 shows the bevel needle and the hollow cannula in combination with a sharpened conical stylet for the drilling. The brachytherapy robot makes it possible to apply a constant rotation and insertion velocity for reproducible experiments on a gel and a beef phantom. The forces necessary for the robot to maintain the pre-set speed were measured and compared. The damage done to the gel phantom was visually evaluated. The rotation of the bevel needle and the rotation of the cannula together with the conical cutting stylet leads to a spiral track. This causes a significant increase of damage in the gel phantom

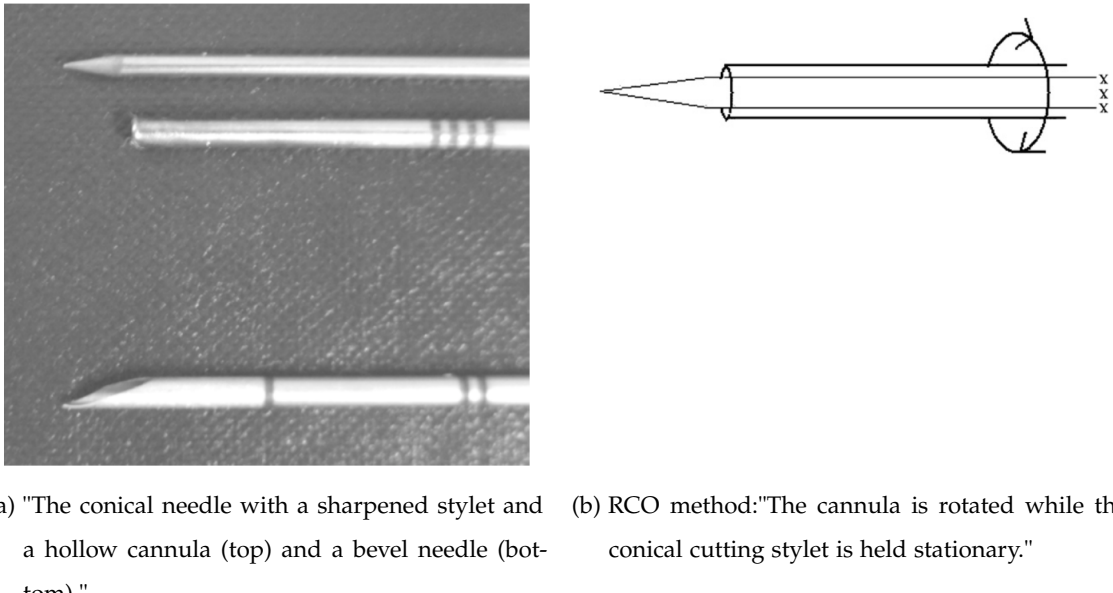


Figure 9: Picture and scheme of investigated needle tips by A Meltsner, Ferrier, and Thomadsen [6]

compared to a classical straight track. The rotate-cannula-only (RCO) method where the cannula is rotated but the stylet is held stationary results in a minimal increase in damage while the insertion force is decreased. Medically speaking, this means less compression of the tissue and consequently less motion of the organ due to needle insertion are increasing the accuracy of the procedure. The combination of insertion and rotation velocity dictate the extend of the damage and have to be investigated for future stylet and cannula configurations.

3.5 APPLICATION TO LIVER METASTASES

Mohnike et al. [5] conducted a study on "Radioablation of liver malignancies with interstitial high-dose-rate brachytherapy" with data from 192 patients in the time intervall of 2006 to 2009 concerning complications and risk factors. Most lesions are treated in a single session while 6 % need several sessions due to their size of more than 10 cm in diameter. Different tumor entities are included with colorectal carcinoma (43 %) and hepatocellular carcinoma (26 %) being the most common ones. About 41 % of the patients have more than one lesion to be treated. Minor and short-term side effects like nausea and vomiting are rather frequent. The overall rate of major complications as bleeding, gastrointestinal ulcers and postinterventional infection is reported to be 4.1 %. This is about the same rate as for radiofrequency

ablation and lower than for surgery. The outcome of this study indicates that interstitial Brachytherapy is advisable for pretreated patients with liver metastases.

It is shown that the application of brachytherapy to liver metastases enriches the spectrum of treatment options without endangering the patient. The development of new needle patterns offering a better sparing of healthy tissue is supported by the progress in robotics enabling the implementation. This work focuses on the calculation of all feasible needle trajectories and ranking needle subsets with a conical shape. This can be done as a pre-calculation step before the treatment. Leaving the final choice of needle tracks to the operator and the dose optimization algorithm makes it widely compatible with different routines.

MATERIALS AND METHODS

This algorithm for computing possible needle trajectories and extracting a list of best entry points is developed along one CT data set of a patient with a liver tumor. In this chapter, the medical assessment of the intervention is discussed first. Section 4.2 describes the basic concept and workflow of the algorithm. Details of the different work sections about input data, computations on the data, output data and their testing are discussed in the following.

4.1 MEDICAL AND ANATOMIC VIEW

First of all, the requirements and risks of image guided HDR treatment on liver metastases have to be defined from a medical point of view. Therefore an internal report was conducted by a physician. The relevant aspects for this work are briefly summarized in the following:

- The number of targets is limited to a maximum of 5 well-defined volumes corresponding to an oligometastatic state of the cancer.
- During the procedure the patient is lying on his back or left side.
- The shortest needle trajectory is generally recommended.
- On the lower side of each rib, intercostal vessels are situated which have to be avoided. No exact distance to the ribs in inferior direction is given, but the access right on the upper side of the ribs is recommended.

4.2 WORKFLOW

In order to meet the requirements described in the previous section, the workflow depicted in figure 10 was developed.

An anatomical scan is required in order to segment the objects of interest: firstly, the skin and the tumor as starting and endpoint of all trajectories, secondly the ribs and blood vessels as obstacles which have to be avoided. The simplest approach to extract feasible trajectories

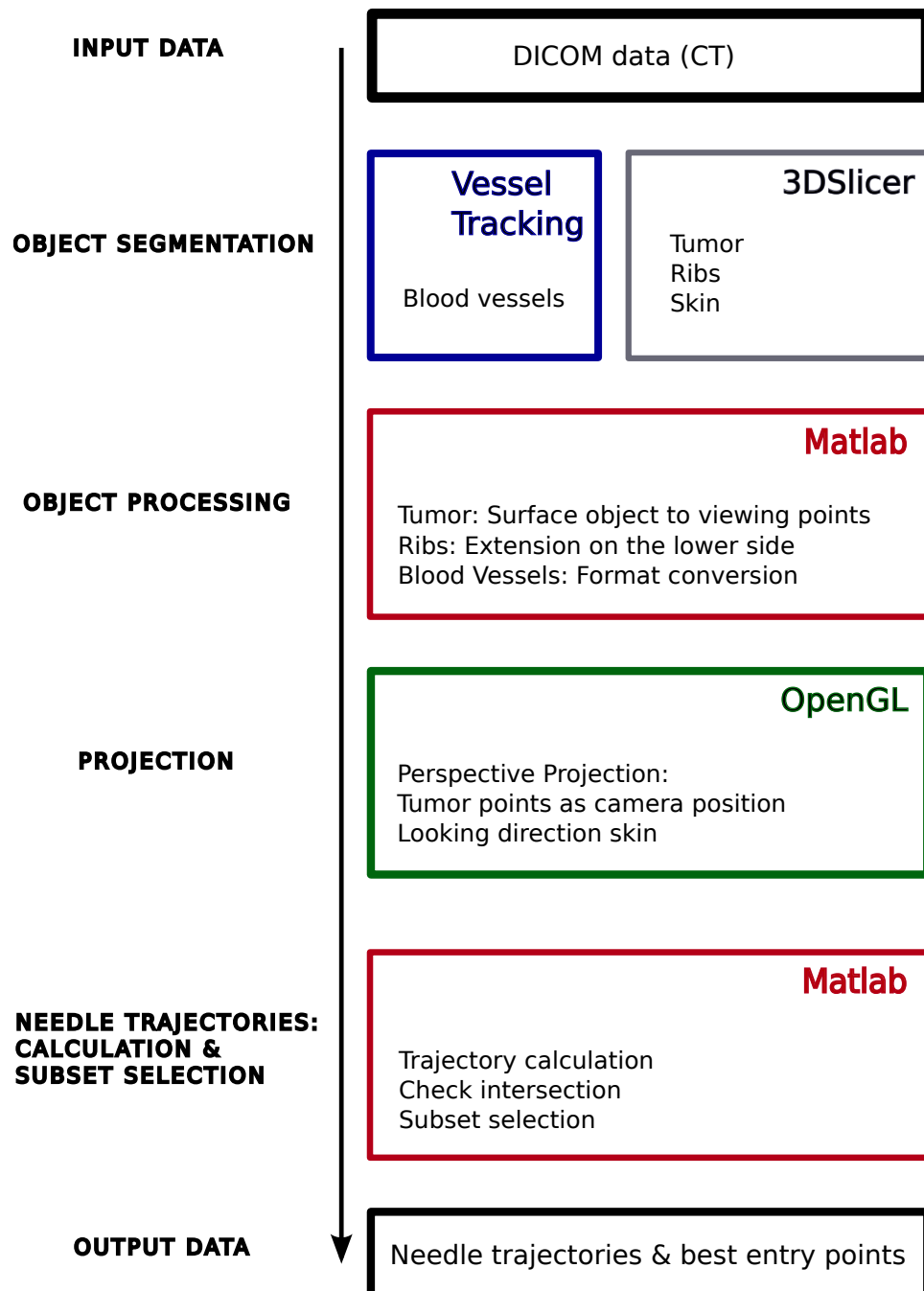


Figure 10: Workflow scheme

would be to define all connecting lines between the skin and the tumor. This set would have to be tested for intersection with the ribs and blood vessels to eliminate the forbidden trajectories. This concept is computationally very expensive and ineffective.

Therefore a graphical solution was developed: The basic idea of the approach of this work is to obtain feasible trajectories by doing perspective projections which can be easily explained by the following example: if a photographer takes a picture of a group, each member of the group can be sure to be visible in the picture if he or she can see the camera. In professional terms, the theory of light field is used. The trajectories are represented by infinitely thin rays of light intersecting two predefined parallel planes. All these trajectories have the four degrees of freedom of a straight line in three dimensional space: one is the distance to the origin, and three stating the direction. The planes are defined in dependence of the tumor and skin objects. To have minimal projective distortion, the tumor plane is chosen to cut through the tumor's center point. The plane approximating the skin has a certain distance such that it is located outside the patient and has a fixed resolution. The common direction of both planes is set according to the generally defined entry zone for liver treatment.

If there is no obstacle in between the intersections of the ray with the planes, the pixel value at the point of intersection with the image plane is assigned to white. If the ray hits an object on its way, the pixel is black, resulting in a binary image. The aim is to determine feasible trajectories from each potential entry point on the patient's skin to the tumor.

The intuitive way to obtain this allocation of entry points and the tumor would therefore be perspective projections from the skin with ray casting to the tumor. This means that the entry zone on the skin has to be exactly defined in advance and many projections have to be executed due to the large number of candidate points on the skin surface. This is inconvenient in terms of clinical routine and computation time. Therefore the projections are chosen to be the other way around, from the tumor point of view. The tumor is well-defined by the segmentation which results in a manageable number of projections for the analysis.

To simplify the projection geometry and minimize distortion, two parallel planes are chosen. One is a plane cutting through the central point of the tumor on which distinct points are selected for the camera position of the projection. The second one is located outside of the patient's body close to the skin where the camera is looking at. Blood vessels and ribs are situated in between. As a result, one gets binary images on the projection plane for each tumor point containing information about which point on the projection plane can be reached from which tumor point.

In the next step the projection images are processed into a common area of all images with a reasonable resolution for brachytherapy treatment. This results in a matrix defining all feasible needle trajectories. As an exemplary model for selecting a subset of needles, the approach of one entry point for a set of needles is chosen. The weighting is realized by two conditions: the full reachability of the tumor and a minimal length of trajectories. A proposal list of best entry points is the result of the subset selection.

4.3 INPUT DATA

As explained in the previous section, an anatomical scan is required. In general, two methods are worth considering: Magnetic Resonance Imaging (MRI) or Computer Tomography (CT). To be able to segment all the mentioned objects, a good contrast for bones, lesions and vessels is crucial. Therefore contrast enhanced CT scans are the most appropriate choice. Admittedly, one problem for the development and testing of this algorithm is that contrast enhancement is not yet routinely used for CT scans of patients with liver metastases. Due to the limitation of time and data access, this work has been developed and tested on one data set: a contrast enhanced CT scan of the upper body in Digital Imaging and Communications in Medicine (DICOM) format with the spatial resolution of $0.67 \times 0.67 \times 1.5 \text{ mm}^3$.

4.4 OBJECT SEGMENTATION

On the basis of the contrast enhanced CT data set, the objects of interest are segmented. In clinical practice, the segmentation of the target and structures at risk is done by a radiation oncologist. For this work, the segmentation was temporarily carried out semi-automatically. The blood vessels were segmented by the implementation of the *** algorithm by another member of the research group. The segmentation of ribs covering the liver, the tumor and the skin surface were realized with various tools of the open source software 3D Slicer Version 4.6.2 listed in Table 2.

The Thresholding tool takes the value of the Houndsfield Unit (HU) of each pixel and divides the image up by an upper and lower threshold. To extract the ribs from the thresholding results, other objects like inner organs with similar HU values are cut out by hand. For the Grow and Cut tool at least two regions have to be marked by hand. In case of the tumor, a region entirely within the tumor and a closed region surrounding the tumor are selected.

Object	Segmentation Tools
Ribs	Thresholding, Cut manually
Tumor	Grow and Cut
Skin	Grow and Cut

Table 2: Segmentation Tools in 3D Slicer Version 4.6.2 used for segmentation of objects

The algorithm iteratively determines the border of those two regions considering the pixel values.

The segmented objects are exported separately in Neuroimaging Informatics Technology Initiative (NIfTI) format as a label maps.

4.5 OBJECT PROCESSING

In this section, the processing of the segmented objects for the projection is described. The objects in NifTI format are loaded into MATLAB Version 2017a and handled with the help of the software package Statistical Parametric Mapping (SPM12) [32] and a 3D geometry toolbox [33]. The blood vessels' object is simply converted to Stereolithography (STL) format and the skin's object is used to define the location of the projection plane by hand. The conversion of the tumor's and the ribs' objects is explained in the following.

4.5.1 Tumor Representation

The tumor surface representation was converted to a voxel representation to get evenly spread points with 1 mm distance to each other in the tumor volume. It was considered to use the voxel center points as viewing points for the projection, but it complicates the processing of the projection images due to different distances to the projection plane resulting in issues with resolutions and distortions. To simplify the situation for a faster and more effective calculation, the voxel center points are projected onto a plane parallel to the projection plane outside of the patient and cutting through the central point of the tumor. This also reduces the number of projections compared to an approach taking the voxel center points.

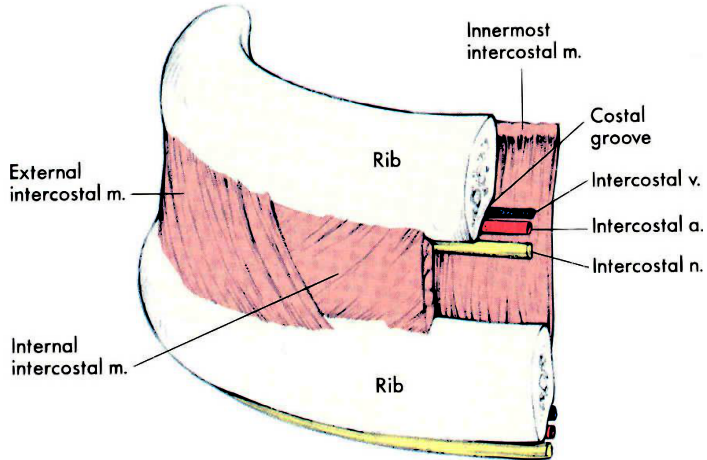


Figure 11: Anatomical sketch of the intercostal space: there are muscles (external, internal and innermost intercostal muscles) in between two ribs and the intercostal vein, artery and nerve right below the costal groove [34].

4.5.2 Ribs' Object

A potential area to insert needles for brachytherapy on liver metastasis is the intercostal space, the space between the ribs. However, there are blood vessels and nerves situated in that area which have to be avoided. Since they lie on the protected lower side of each rib this area has to be excluded from the potential region where a needle can pass through. First, it was considered to take that into account in the step of processing all projection images. Since all of them have the ribs represented as black strips in it, a band-pass filter only allowing a small area above each rib could be applied. A major problem however was the different distortion for each viewing point which made it difficult to select the exact same region above the ribs for all projections. A more practical way to translate the condition into the workflow was to expand the ribs' object to this area before any projection images are taken.

The ribs' surface object is represented by a list of vertices and corresponding faces. To extract the concerned region, one needs to find the faces on the lower side of the ribs. Therefore, the face normals are calculated and those with a component in negative z-direction are selected. These normals are normalized to the unit length of 1 mm and then multiplied by a factor n_{extend} . The vertices which are the corners of the selected faces are shifted by the manipulated face normals. This leads to a safety margin of n_{extend} mm to protect the vessels below the ribs (figure 12).

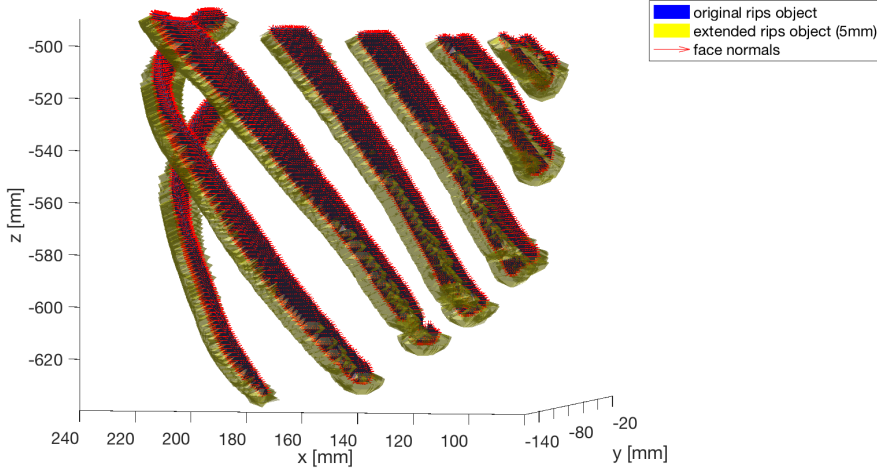


Figure 12: Extension of the ribs' object: the face normals are extracted from the originally segmented ribs (blue) and normalized (red arrows). With an extension factor $n_{\text{extend}} = 5 \text{ mm}$ the extended ribs' object (semi-transparent yellow) is generated.

4.6 PROJECTION

The aim of this work section is to allocate points on the patient's surface to points within the liver tumor such that the trajectory connecting the two points do not penetrate any restricted region in between. The concept to obtain this is to project the scene in Open Graphics Library (OpenGL) with a virtual camera situated in distinct points in the tumor looking at the patient's surface with obstacles like blood vessels and the ribs.

Since the ribs, the area right below each rib and the blood vessels in the liver can or must not be penetrated by the brachytherapy needle, the derived objects have to be included in the projection. From the STL files of the objects the surface vertices are loaded into OpenGL and chosen to be represented as black polygon surfaces while the background is white. This leads to black areas on the projection image where the trajectory from the tumor to the point on the projection plane does not meet the condition of avoiding the previously defined objects. The projection of the scene captures the image after a coordinate transformation. The transformation matrix (*MVP*) is composed by three matrices (Listing 1). The first one is the *Model Matrix* that assigns the model to the world coordinates. The second one defines the camera position and viewing direction (*Camera Matrix*). The third one, *Projection Matrix*, defines the camera settings like the field of view.

The *Model Matrix* is set to be the identity matrix which means that all objects have the same coordinates in the OpenGL world as they have in their object files and the original CT image.

For the calculation of the *Camera Matrix* the `lookAt` function of the OpenGL Mathematics (GLM) library is used. The input arguments are three vectors with x-, y- and z-coordinate. `CameraPos` is the position of the virtual camera which is chosen to be the projected points on the central tumor plane. `CenterLookAt` is the point where the camera is looking at, so a point on the projection plane right outside the patient's body. The third input vector defines which way is up or down. In this case the z-axis is chosen to define the upwards direction. The *Projection Matrix* is calculated with the GLM function `perspective` which takes the angle for field of view, a width to height ratio and the display range as input arguments. The field of view is set to 120 deg. The width to height ratio is chosen to be 1:1 to avoid distortion. The display range is defined by a near and a far clipping plane which are set such that the whole scene with all the objects lies in between. The OpenGL window size is set to 1000×1000 pixels defining the resolution of the projection image. A snippet of the function is shown in listing 1.

```
// Camera View
glm::mat4 CameraMatrix = glm::lookAt(
    CameraPos, // the position of your camera, in world space
    CenterlookAt, // where you want to look at, in world space
    glm::vec3(0,0,1) // the axis which is defined as upwards
);

// Projection matrix : 120 deg = 2.0944 rad Field of View, 1:1 ratio, display
// range : 0.1 unit <-> 1000 units
glm::mat4 Projection = glm::perspective(2.0944f, 1.0f / 1.0f, 0.1f, 1000.0f);

// Model matrix : an identity matrix (model will be at the origin)
glm::mat4 Model      = glm::mat4(1.0f);

// Compute the MVP matrix
glm::mat4 MVP        = Projection * CameraMatrix * Model;
```

Listing 1: C++/OpenGL code snippet of functions used for the projection

The output of the OpenGL projection program is a number of binary images each corresponding to one of the projected points on the tumor plane saved in Truevision Graphics Adapter (TGA) format. An exemplary projection image will be presented in chapter 5.

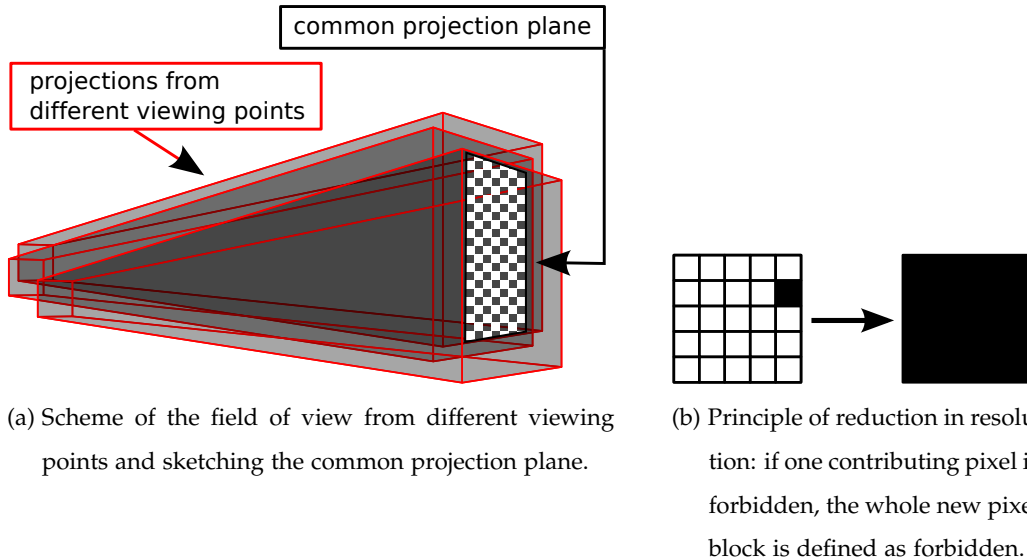


Figure 13: Processing projection images to needle trajectories

4.7 CALCULATION OF TRAJECTORIES

At this point, the projection images are captured which contain information about which tumor point can reach which pixel of their individual projection plane. The viewing direction from the tumor points is parallel resulting into shifted projection images on the projection plane. Only for the area which is common in all projections a statement can be made whether the point reaches each tumor point by an allowed trajectory or not. Therefore the images are loaded into MATLAB Version 2017a where the common projection area was extracted (figure 13a).

In that image cut-out, a reasonable common resolution has to be defined. Due to the shift, the images do not have the same pixel positions. Furthermore, the resolution is higher than necessary for the implementation for brachytherapy and should to be reduced. Because of the needle diameter of about 1 – 2 mm and the limited precision of the surgeon's needle placement, a resolution of about $1 \times 1 \text{ mm}^2$ of the projection plane is reasonable. The resolution for the projections is chosen to be about 5 times higher to make sure that the infinitely thin light rays do not miss small critical structure in between their paths. For the example in figure 13b a light ray intersecting the coarse pixel in the center would have classified it as a feasible entry point for a trajectory. With the high resolution in the projection and the reduction in this work stage, it is rightly infeasible.

As a result one gets a matrix with the coordinates of common pixels and a second matrix

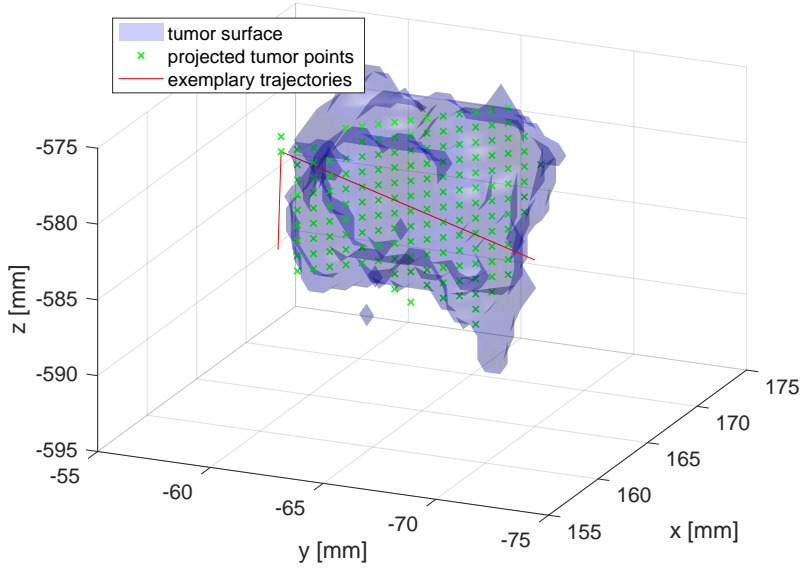


Figure 14: Two exemplary trajectories (red) reaching the same tumor point (green). One intersects the tumor volume (blue), one passes by.

with the binary information about each of the projections correspondingly.

For simplification the tumor volume was perpendicularly projected onto the plane before using it as the viewing point for the projection of the scene. The points on the edges of the tumor might be reached by oblique trajectories that do not intersect the tumor volume (figure 14). This has to be tested in order to eliminate not intersecting trajectories from the potential list of needles.

4.8 WEIGHTING AND NEEDLE SUBSETS

The aim of this work is not only to calculate all the possible trajectories but also to give an example of how to rank them for the subsequent dose calculation algorithm. There are several reasonable conditions which can be used for such a ranking. As stated in the medical requirements, short needle trajectories are desirable. Also the angle of the needle trajectories could be used as a criterion as for example for the current state of the art with parallel needle templates facilitating fast and stable needle insertion. The distance to structures at risk and the ribs for additional safety margins or as few entry points as possible to reduce the risk of inflammation are further potential restrictions. On the current output of feasible needle

trajectories various conditions could be applied to select a subset.

As an example the shortest length of needle trajectories in combination with the restriction to one entry point is chosen. Therefore, those pixels in the projection images which can be reached from all points on the tumor plane are selected and the sum of all their trajectory lengths is used for ranking the entry points. To avoid the accumulation of several entry points very close to each other, a minimum distance of 1 cm is set between the points which make the list of the 5 best needle insertion points.

4.9 PROJECTION PLANE TO PATIENT SURFACE

All calculations are done so far for a regular pixel array and not on the real surface of the patient because it was fast and easy. To allocate the selected needle insertion points to the real coordinates on the patient's surface, the polygon grid representing the skin is perpendicularly projected onto the projection plane as well. With a search of the closest projected surface point to the calculated best needle insertion points, the final list in the coordinate system of the original CT image can be determined.

4.10 OUTPUT DATA

The results of the algorithm are two matrices and a list. Let $n \times n$ be the downsampled resolution of the common projection plane and m be the number of tumor points, e.g. number of projections.

- One matrix with the dimensions $n \times n \times 3$ containing the x-, y-, z-coordinates of each pixel point of the common projection plane.
- A corresponding matrix $n \times n \times m$ containing binary information about which pixel can be reached from the tumor point.
- A list with the coordinates of best entry points on the skin surface from which the whole tumor can be reached in the shortest distance possible.

4.11 EVALUATION

Since there is no other similar method against which results can be compared, a brief evaluation of the computation time and the ribs extension factor is done in addition to a general visual evaluation of the processing steps and the result.

4.11.1 Computation Time

All calculations were executed on a MacBook Pro with a 2,4 GHz Intel Core i7 Processor and 16 GB 1600 MHz DDR3 Memory. The time measurement for the computations in Matlab were done with the `profile` function, while in OpenGL the `std::clock()` function was used.

4.11.2 Workflow Output

The extension factor n_{extend} of the ribs' object is heuristically chosen with the aim to extract for the intercostal space only points right above a rib, but not generally prohibiting the entry between ribs. To investigate its influence on a reasonable output of the workflow, two different factors are picked: 5 mm and 10 mm. The result is visually evaluated and discussed in the following chapters.

RESULTS

This chapter presents the qualitative result of the developed algorithm and some interims result of the computation process. A visualization of the segmented objects and their processing is shown. After the projections, the trajectory calculation is done. The best entry point list depending on two different extension factors for the ribs' object are compared in the following. At last, the computation time is presented.

5.1 OBJECT PROCESSING AND PROJECTION

Figure 15 shows the visualization of the scene with the segmented objects. The coordinate system is passed on from the original DICOM data set.

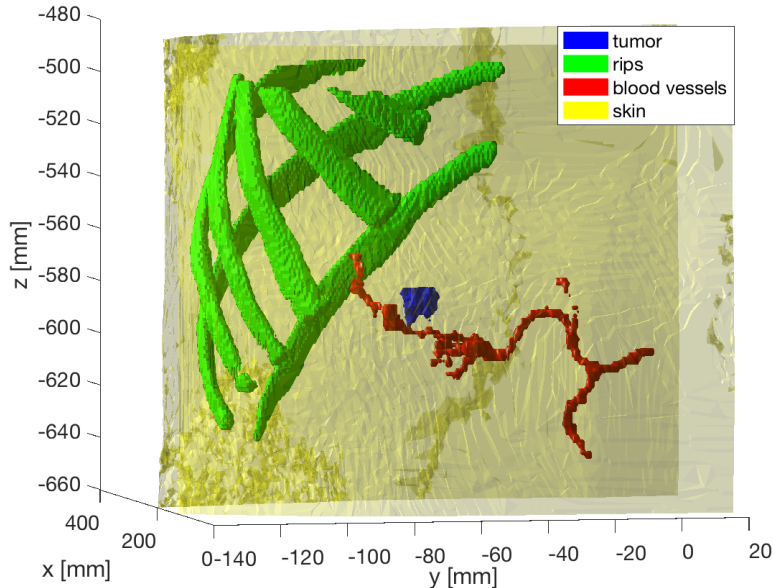


Figure 15: Surface representation of the scene with the tumor (blue), blood vessels (red), ribs (green) and the skin (yellow) as they were segmented.

In the first computation block in Matlab, the tumor object is processed. The surface representation (figure 16a) is converted into voxels of $1 \times 1 \times 1 \text{ mm}^3$. The center points of the

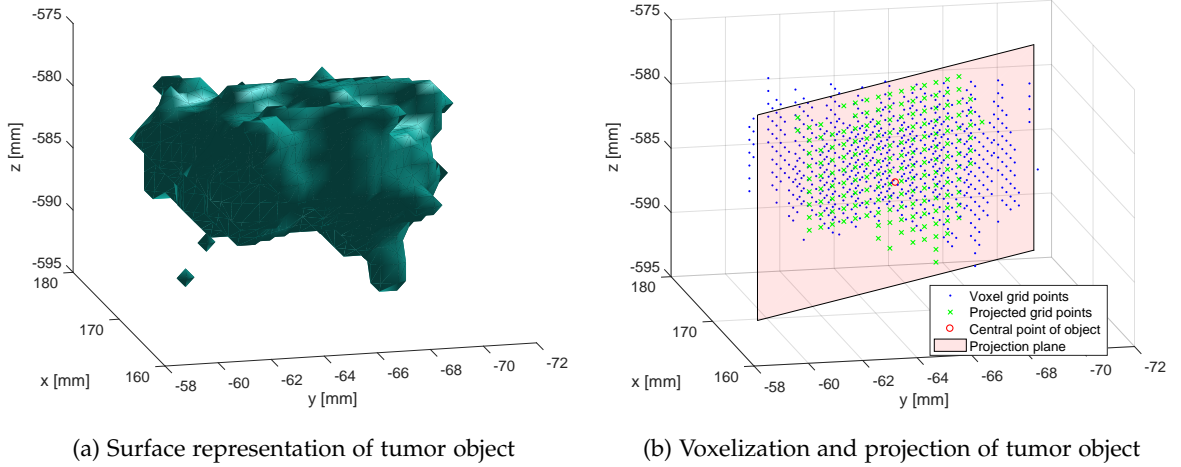


Figure 16: Tumor object in two different representations

tumor's voxels are represented in blue in figure 16b. The plane containing the center point (red circle) and with the normal vector $[-1, -1, 0]$ is drawn in semi-transparent magenta. The projected points on the plane are represented in green and have a spacing of 1 mm corresponding to the previously defined voxel size. The initial resolution of the acquired DICOM image was $0.67 \times 0.67 \times 1.5 \text{ mm}^3$ which limits the resolution of the computation to the same range. The spacing of 1 mm was chosen heuristically to get a reasonable number of points in the tumor plane in a computational manner, covering the volume correspondingly to general dose calculation resolutions and needle diameter.

The segmented object of the ribs was extended in the next step. In figure 17 the originally segmented object is opaque while the extension is semi-transparent. Two extension factors are selected to explore the influence on the final result: 5 mm and 10 mm. Projection images generated in OpenGL are shown as an example for both extension values from the same, arbitrary projected tumor point in figure 18.

The scene with all relevant objects for the algorithm is plotted in figure 19a. The projected points on the central tumor plane are shown in blue. The viewing direction in OpenGL was chosen to be the same as the orientation of the tumor plane. Together with the selection of the distance between both planes, the projection plane is generated as depicted in magenta. Blood vessels and expanded ribs are involved in the projection.

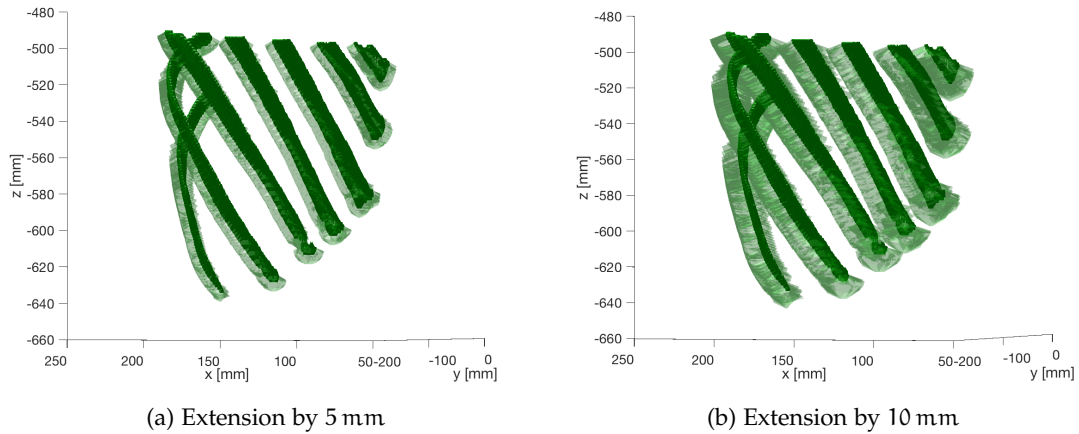
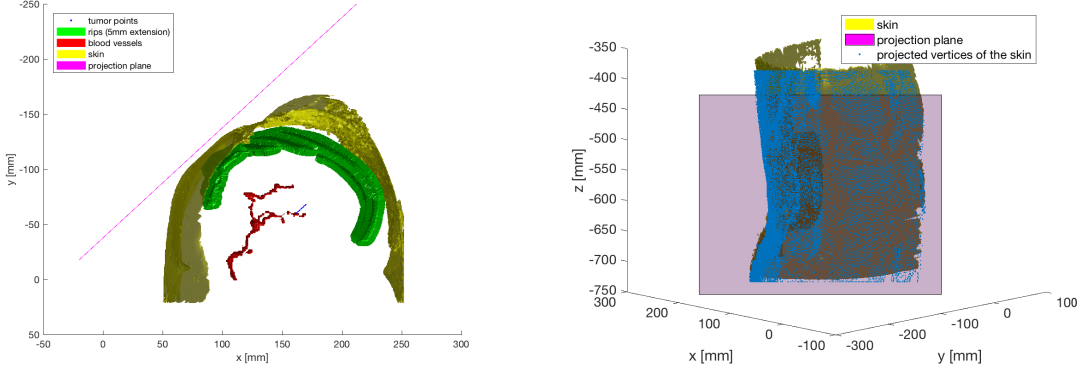


Figure 17: Surface object representing the ribs: The opaque objects are the originally segmented ribs, the extension is plotted semi-transparent. Two different extension factors are selected to investigate its influence on the result.



Figure 18: Exemplary projection images with the viewing position [168.25, -65.95, -579.65]



(a) Top view of the projection scene: the projected points on the tumor plane (blue) lie on a plane parallel to the projection plane (magenta). The blood vessels (red) and the expanded ribs (green) are the obstacles. The patient’s skin surface (yellow) is shown for the sake of completeness of the scene.

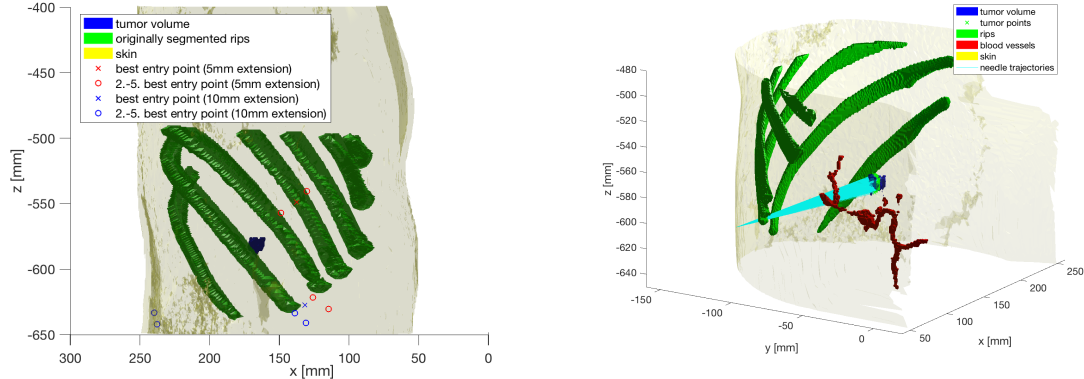
(b) Perpendicular view on the projection plane (semi-transparent magenta) with the vertices of the skin’s object (yellow) projected on it (blue dots).

Figure 19: Visualization of the scene: (a) with all relevant objects, points and planes of the algorithm, (b) projection of skin surface onto projection plane

5.2 TRAJECTORY CALCULATION AND SUBSETS

The skin surface is relevant for the final list of entry points which are calculated on the projection plane, but have to be transferred on the skin surface. Therefore, another projection is done in Matlab: skin surface onto projection plane. This provides an association of the vertices of the skin surface object to the pixel points on the projection plane. The skin surface is curved which leads to an increasing distance between skin and projection plane when moving along the x- and y-direction. Figure 19b exposes the irregularity of the projected points on the plane.

The best entry points for both extension factors are displayed in figure 20a. For the visual evaluation, the tumor volume, ribs and skin are shown as well. The crosses in red (5 mm extension) and blue (10 mm extension) represent the first entry on the list of best entry points. For the red one, the trajectories pass through the intercostal region right under a rib. Two other entry points for the smaller extension are located on the upper side of ribs. None of the blue entry points lie between ribs. Two points are even on the back side of the patient. The threshold of 1 cm between entry points prevent an accumulation of the entry points, but



(a) Transversal view of the scene: the selected entry points for both extension factors are displayed in the context of the patient's skin, ribs and tumor.

(b) All trajectories from one entry point on the skin (yellow) to the projected tumor points (green) not intersecting the ribs(green) and blood vessels

Figure 20: Presentation of the computation results: (a) all selected entry points, (b) all trajectories from one entry point.

a pattern can be observed from two points for both extension factors in the prolongation of the second and third lowest rib.

5.3 CALCULATION TIME

The result of the time measurement of all steps of the workflow are displayed in table 3. The total computation time is 3.71h. The greatest share of the total time consumption is associated with the check whether a potential needle trajectory crosses the tumor volume or misses it. The share of potential trajectories which are eliminated by this check is 0.96 %. The second largest share is used for the calculation of all feasible trajectories from projection images. All other computations take less than 1 min.

Computation step	Computation time	Share of computation block time	Share of total computation time
Total computation time	13362 s		100 %
Matlab: Object processing for Projection	61.6 s	100 %	0.46 %
Tumor object to points on plane	26.2 s	42.5 %	0.20 %
Blood vessel nifti to stl	13.9 s	22.6 %	0.10 %
Expand ribs' object	21.5 s	34.9 %	0.16 %
OpenGL: Projections	31.1 s	100 %	0.23 %
Matlab: Projection images to needle subset	13269.6 s	100 %	99.31 %
Projection Image to all needle trajectories	1628.9 s	12.3 %	12.19 %
Check intersection of trajectories with tumor volume	11584.8 s	87.3 %	86.70 %
Needle subset selection	55.8 s	0.4 %	0.4 %

Table 3: Computation time for the steps in the algorithm. The first column describes what is done in the computation step (further explanations in chapter 4). The calculation time for the extension of the ribs by 5 mm was taken, because there was no significant difference to the factor of 10 mm. The absolute time is given in the second column. The third and fourth column show the relative time consumption to the computation block and the overall computation time.

DISCUSSION

In the following, the results presented in the previous chapter are discussed by their issues. The specific implementation problems of the tumor and skin projection as well as the choice of the ribs' extension factor are treated first. Then the distribution of computation time and possible improvements are dealt with. At last, the current limitations and automation of the algorithm is stated.

6.1 TUMOR PROJECTION

In order to make the computation faster and easier, the tumor object is projected on its central plane first. The projected points are used as viewing points for the projection. This causes an additional computation step after the calculation of trajectories, where it must be checked whether the needle really enters the tumor volume or if it is an error due to the reduction of a volume to a plane.

If the volume projected on a plane containing the central point was a sphere, all trajectories cutting the plane in a projected point would also cut the volume. An option to eliminate the checking step which consumes the greatest part of the computation time, would therefore be to replace the tumor object by an enclosing sphere. If the tumor shape is highly irregular, this would lead to a big increase of volume for the altered tumor object and projected points resulting into more projections and calculations in the following.

Alternatively, instead of projected points, the voxel center points of the tumor could be used for the projections. This has the same disadvantage of increasing the number of projections and it complicates the geometry for the trajectory calculations.

Simpler improvements of the current state would be a faster intersection check by parallelization or with a specialized software. It could also be considered to move this check to the end of the whole computation and only execute it for the trajectories of selected entry points.

Another way to check whether a trajectory is intersecting or not could be to do additional projections of the tumor object: the same viewing points are chosen as before and the tumor

is loaded as a surface object into OpenGL instead of the ribs or blood vessels. A perspective projection is done with the original and in the opposite looking direction. If the whole projection image is black, all trajectories cut the tumor. If there are white pixels, the corresponding trajectories were falsely classified as feasible. An overlay of these images with the actual projection images contain only the truly intersecting and allowed needle trajectories.

6.2 RIBS' EXTENSION FACTORS

Two extension factors n_{extend} were chosen to investigate the influence of this parameter on the results. According to medical routines, entry points right above a costal arches are desirable. The challenge is to find an intermediate factor such that the vessels on the lower side of the ribs are protected but the intercostal space is not completely blocked from potential needle trajectories. The extension of 10 mm lead to this total blockage. The resulting entry point proposals are not suitable. The factor of 5 mm produced better results. Two of the five proposed entry points are right on the upper side of a costal arch. However, the entry point computed as the best one, is close to the lower side of a rib which is not permitted. This could be a result of the problematic transfer from the projection plane to the skin surfaced discussed in section 6.3. A test with different factors in this order of magnitude should be conducted to find a trade-off between these boundary conditions. The influence of the minimal distance between entry points set to 1 cm on the distribution of entry points should also be evaluated.

6.3 SKIN PROJECTION

Close to the center point of the projection plane, which is also the closest area to the tumor, the skin projection is an acceptable first approximation that allows easy and fast calculations. For greater distances from that point, it causes increasing inaccuracy. The choice of location and orientation of the projection plane is therefore important and has to be adapted to the tumor site and the patient's anatomy.

An improvement would be to use a curved plane adapted to the patient's surface curvature, which raises difficulties with distortion of the grid on that projection plane. A second problem is the uneven spread of the projected vertices over the plane. To take a random sam-

ple of points distributed over the skin surface could fix these irregularities and raise accuracy for the entry point selection.

6.4 COMPUTATION TIME

The biggest time consumer in the algorithm is the check of trajectory intersection with the tumor volume as discussed in 6.1. On the one hand, an implementation in a more sophisticated and faster language can speed up the calculation. On the other hand, it is not necessary at this point to accelerate this algorithm to real-time planning speed, because it is intended as a pre-computation step in advance to the intervention.

6.5 LIMITATIONS

At the moment, the algorithm can compute the needle trajectories and the entry points only for one target volume at a time. With little adjustments, there can be one computation for several metastases. However, the best entry point calculation only works with the strict condition that all tumor points have to be reached from one entry point. If the target is located such that it is generally impossible to hold that constraint, no proposal of entry points can be given. This means, that the algorithm is currently limited to an intermediate size of the target volume with a non-problematic location, for example not to close to the ribs or the blood vessels.

Another limitation is currently given by the dependency on a blood vessel tracking algorithm which has not been extensively tested yet. Only one data set is available for this approach. Other options to obtain the segmented blood vessels in the liver should be considered.

6.6 AUTOMATION

The algorithm consists of several separate computation steps with different software. After the manual segmentation of objects, the program parts in Matlab, OpenGL and Matlab again run each automatically. This allows for easy adjustments on the computations at the moment. With a wrapper script, the whole program could run sequentially. However, the use of different softwares leads to a massive production of data which could be avoided

if all computations would be unified in one program. C++, which is already used for the OpenGL implementation, offers a universally usable platform avoiding software license and version issues with Matlab. A translation of the prototype version from Matlab to C++ is consequently a step towards better usability and automation for clinical application. The segmentation should be done by the physician in a clinically tested software environment.

CONCLUSION AND OUTLOOK

The presented algorithm is a first prototype for pre-calculating the needle trajectories and proposing best entry points for a dose planning algorithm. It was shown, that the computation delivers a reasonable output depending on heuristically chosen parameters like the ribs' extension.

These choices have to be further investigated. Furthermore, the projection geometry has to be revised and improved to achieve more accuracy. A translation from Matlab into C++ would unify the computation steps in one program eliminating the need for intermediate storage in different file formats. This reduces the required memory, speeds-up the computation as a whole and makes it more robust. It would also be desirable to extend the computation limited to one target volume at the moment to the proposal of as few entry points as possible.

In order to test the output quantitatively, a dose calculation should be appended. The influence on the choice of needles with the proposed ranking has to be compared against other needle selection algorithms. The aim is to reduce the number of needles necessary to deliver the prescribed dose to the target volume while sparing the normal tissue from mechanical damage. Other selection rules than the one-entry-point-approach could be implemented in order to compare the impact of different needle patterns on the treatment plan for liver metastases. In clinical studies the gain of each approach should be explored.

Brachytherapy of liver metastases has already been proven to be a useful supplement in the spectrum of treatment options. Since it is applicable to inoperable sites, an accurate planning and implementation is crucial. With this objective, a brachytherapy robot translating a plan with excellent precision is the next evolutionary step demanding a high degree of computational automation. This work provides a prototype of a new approach to reach that goal.

BIBLIOGRAPHY

- [1] WHO. *World wide cancer statistics fact sheet on liver cancer*. Nov. 2017. URL: http://globocan.iarc.fr/Pages/fact_sheets_cancer.aspx?cancer=liver.
- [2] Nabil Ismaili. „Treatment of colorectal liver metastases“. In: *World Journal of Surgical Oncology* 9.1 (Nov. 2011), p. 154. ISSN: 1477-7819.
- [3] Jeffrey F Williamson. „Brachytherapy technology and physics practice since 1950: a half-century of progress“. In: *Physics in Medicine and Biology* 51.13 (2006), R303.
- [4] Timm Denecke and Enrique Lopez Hänninen. „Brachytherapy of liver metastases“. In: *Pancreatic Cancer* (2008), pp. 95–104.
- [5] Konrad Mohnike et al. „Radioablation of liver malignancies with interstitial high-dose-rate brachytherapy : Complications and risk factors“. In: 192 (Feb. 2016).
- [6] M A Meltsner, Nicola Ferrier, and Bruce Thomadsen. „Observations on rotating needle insertions using a brachytherapy robot“. In: 52 (Nov. 2007), pp. 6027–37.
- [7] Timmy Siauw, Adam Cunha, Dmitry Berenson, Alper Atamtürk, I-Chow Hsu, Ken Goldberg, and Jean Pouliot. „NPIP: A skew line needle configuration optimization system for HDR brachytherapy“. In: *Medical Physics* 39.7Part1 (2012), pp. 4339–4346.
- [8] Jens Ricke and Peter Wust. „Computed Tomography–Guided Brachytherapy for Liver Cancer“. In: *Seminars in Radiation Oncology* 21.4 (2011). Radiation Therapy of Primary and Metastatic Liver Tumors, pp. 287 –293. ISSN: 1053-4296.
- [9] Gopal B. Saha. *Physics and Radiobiology of Nuclear Medicine*. eng. Third Edition. Springer-Link : Bücher. New York, NY: Springer New York, 2006, Online–Ressource (XVI, 320 p. 111 illus, digital).
- [10] Kátia A. Fonseca, Marina F. Koskinas, and Mauro S. Dias. „Disintegration rate measurement of a ^{192}Ir solution“. In: *Applied Radiation and Isotopes* 54.1 (2001), pp. 141 – 145. ISSN: 0969-8043. DOI: [https://doi.org/10.1016/S0969-8043\(00\)00158-5](https://doi.org/10.1016/S0969-8043(00)00158-5). URL: <http://www.sciencedirect.com/science/article/pii/S0969804300001585>.
- [11] *Plot of Iridium gamma-spectrum*. 2017. URL: <https://www.nucleonica.com/wiki/index.php?title=File%3AFig5.14.jpg>.

- [12] *Photon attenuation in water from NIST data base*. 2017. URL: https://physics.nist.gov/cgi-bin/Xcom/xcom3_2.
- [13] Prabhakar Ramachandran. „New era of electronic brachytherapy“. In: *World Journal of Radiology* 9.4 (Apr. 2017), pp. 148–154.
- [14] Carlos A. Perez, Srinivasan Vijayakumar, Seymour H. Levitt, and James A. Purdy. *Technical Basis of Radiation Therapy. Practical Clinical Applications*. eng. 4th Revised Edition. SpringerLink : Bücher. Berlin, Heidelberg: Springer Berlin Heidelberg, 2006, Online-Ressource (XIII, 861 p. 507 illus. in 799 sep. illus., 175 in color, 146 tabs, digital).
- [15] Phillip M. Devlin, ed. *Brachytherapy: Applications and Techniques*. 1st ed. Lippincott Williams and Wilkins, 2007.
- [16] Alfredo Polo, Carl Salembier, Jack Venselaar, and Peter Hoskin. „Review of intraoperative imaging and planning techniques in permanent seed prostate brachytherapy“. In: *Radiotherapy and Oncology* 94.1 (2010), pp. 12 –23.
- [17] Subir Nag, Jay P Ciezki, Robert Cormack, Stephen Doggett, Keith DeWyngaert, Gregory K Edmundson, Richard G Stock, Nelson Stone, Yan Yu, and Michael J Zelefsky. „Intraoperative planning and evaluation of permanent prostate brachytherapy: Report of the American Brachytherapy Society“. In: 51 (Jan. 2002), pp. 1422–30.
- [18] D.Allan Wilkinson, Eric J Lee, Jay P Ciezki, Das Mohan, Craig Zippe, Kenneth Angermeier, James Ulchaker, and Eric A Klein. „Dosimetric comparison of pre-planned and or-planned prostate seed brachytherapy“. In: *International Journal of Radiation Oncology*Biology*Physics* 48.4 (2000), pp. 1241 –1244.
- [19] Thomas G Shanahan, Parashar J Nanavati, Paul W Mueller, and Randy B Maxey. „A comparison of permanent prostate brachytherapy techniques: preplan vs. hybrid interactive planning with postimplant analysis“. In: *International Journal of Radiation Oncology*Biology*Physics* 53.2 (2002), pp. 490 –496.
- [20] Nathanael Kuo, Ehsan Dehghan, Anton Deguet, Omar Y. Mian, Yi Le, E. Clif Burdette, Gabor Fichtinger, Jerry L. Prince, Danny Y. Song, and Junghoon Lee. „An image-guidance system for dynamic dose calculation in prostate brachytherapy using ultrasound and fluoroscopy“. In: *Medical Physics* 41.9 (2014). 091712, 091712–n/a.
- [21] H.H. Holm, N. Juul, J.F. Pedersen, H. Hansen, I. Strøyer, and Harry W. Herr. „Transperineal ^{125}I odine seed implantation in prostatic cancer guided by transrectal ultrasonography“. In: *The Journal of Urology* 167.2, Part 2 (2002), pp. 985 –988.

- [22] M. Sean Peach, Daniel M Trifiletti, and Bruce Libby. „Systematic Review of Focal Prostate Brachytherapy and the Future Implementation of Image-Guided Prostate HDR Brachytherapy Using MR-Ultrasound Fusion“. English. In: *Prostate Cancer* 2016 (2016), pp. 1–13.
- [23] Anthony V. D'Amico, Robert Cormack, Clare M. Tempany, Sanjaya Kumar, George Topulos, Hanne M. Kooy, and C. Norman Coleman. „Real-time magnetic resonance image-guided interstitial brachytherapy in the treatment of select patients with clinically localized prostate cancer“. In: *International Journal of Radiation Oncology *Biology *Physics* 42.3 (1998), pp. 507–515.
- [24] Christophe Reynier, Jocelyne Troccaz, Philippe Fourneret, André Dusserre, Cécile Gay-Jeune, Jean-Luc Descotes, Michel Bolla, and Jean-Yves Giraud. „MRI/TRUS data fusion for prostate brachytherapy. Preliminary results“. In: *Medical Physics* 31.6 (2004), pp. 1568–1575.
- [25] Jens Ricke et al. „CT-guided interstitial brachytherapy of liver malignancies alone or in combination with thermal ablation: phase I–II results of a novel technique“. In: *International Journal of Radiation Oncology *Biology *Physics* 58.5 (), pp. 1496–1505.
- [26] Tibor Major, Georgina Fröhlich, Katalin Lövey, János Fodor, and Csaba Polgár. „Dosimetric experience with accelerated partial breast irradiation using image-guided interstitial brachytherapy“. In: *Radiotherapy and Oncology* 90.1 (2009), pp. 48–55.
- [27] Eric Poulin, Charles-Antoine Collins Fekete, Mélanie Létourneau, Aaron Fenster, Jean Pouliot, and Luc Beaulieu. „Adaptation of the CVT algorithm for catheter optimization in high dose rate brachytherapy“. In: *Medical Physics* 40.11 (2013). 111724, 111724–n/a.
- [28] Qiang Du, Vance Faber, and Max Gunzburger. „Centroidal Voronoi Tessellations: Applications and Algorithms“. In: *SIAM Rev.* 41.4 (Dec. 1999), pp. 637–676.
- [29] J Adam Cunha, I-Chow Hsu, and Jean Pouliot. „Dosimetric equivalence of nonstandard HDR brachytherapy catheter patterns“. In: 36 (Feb. 2009), pp. 233–9.
- [30] Animesh Garg, Timmy Siauw, Guang Yang, Sachin Patil, J. Adam M Cunha, I-Chow Hsu, Jean Pouliot, Alper Atamturk, and Ken Goldberg. *Exact reachability analysis for planning skew-line needle arrangements for automated brachytherapy*. English. IEEE, 2014, pp. 524–531.

- [31] Gang Wan, Zhouping Wei, Lori Gardi, Donal B. Downey, and Aaron Fenster. „Brachytherapy needle deflection evaluation and correction“. In: *Medical Physics* 32.4 (2005), pp. 902–909.
- [32] *Matlab toolbox: SPM12*. 2017. URL: <http://www.fil.ion.ucl.ac.uk/spm/>.
- [33] *Matlab toolbox: TBGeom3D*. URL: <https://de.mathworks.com/matlabcentral/fileexchange/24484-geom3d>.
- [34] *Anatomy sketch: intercostal space*. URL: <https://www.n30.com/resource/64467/intercostal-muscles-pmg-biology-intercostal-space.jpg>.

ERKLÄRUNG

Ich versichere, dass ich diese Arbeit selbstständig verfasst und keine anderen als die angegebenen Quellen und Hilfsmittel benutzt habe.

Heidelberg, den 17. Januar 2018,

Johanna Stratemeyer

COLOPHON

This document was typeset using the typographical look-and-feel `classicthesis` developed by André Miede. The style was inspired by Robert Bringhurst's seminal book on typography "*The Elements of Typographic Style*". `classicthesis` is available for both L^AT_EX and LyX:

<https://bitbucket.org/amiede/classicthesis/>

Happy users of `classicthesis` usually send a real postcard to the author, a collection of postcards received so far is featured here:

<http://postcards.miede.de/>

Final Version as of 17. Januar 2018 (classicthesis version 1).